Geophysical Research Letters

RESEARCH LETTER
10.1029/2020GL087319

Cold Pools as Conveyor Belts of Moisture

Herman F. Fuglestvedt[1,2] **and Jan O. Haerter**[2,3,4]

[1]Department of Geosciences, University of Oslo, Oslo, Norway, [2]Niels Bohr Institute, University of Copenhagen, Copenhagen, Denmark, [3]Complexity and Climate, Leibniz Centre for Tropical Marine Research, Bremen, Germany, [4]Physics & Earth Sciences, Jacobs University Bremen, Bremen, Germany

Key Points:
- Cold pool collisions cause a sustained reset of boundary layer circulation
- Tracking of colliding outflow boundaries highlights the role of premoistening in cold pool-driven convective organization
- The primary cause of premoistening is sustained low-level convergence, surface fluxes play a secondary role

Supporting Information:
- Supporting Information S1

Correspondence to:
H. F. Fuglestvedt,
herman.fuglestvedt@geo.uio.no

Citation:
Fuglestvedt, H. F., & Haerter, J. O. (2020). Cold pools as conveyor belts of moisture. *Geophysical Research Letters*, *47*, e2020GL087319. https://doi.org/10.1029/2020GL087319

Received 25 FEB 2020
Accepted 20 MAY 2020
Accepted article online 28 MAR 2020

Abstract

Observations and simulations have found convective cold pools to trigger and organize subsequent updrafts by modifying boundary layer temperature and moisture as well as by lifting air parcels at the outflow boundaries. We study the causality between cold pools and subsequent deep convection in idealized large-eddy simulations by tracking colliding outflow boundaries preceding hundreds of deep convection events. When outflow boundaries collide, their common front position remains immobile, whereas the internal cold pool dynamics continues for hours. We analyze how this dynamics "funnels" moisture from a relatively large volume into a narrow convergence zone. We quantify moisture convergence and separate the contribution from surface fluxes, which we find to play a secondary role. Our results highlight that dynamical effects are crucial in triggering convection, even in radiative-convective equilibrium. However, it is the low-level convergence resulting from this dynamics that removes inhibition, moistens the atmosphere aloft, and ultimately permits deep convection.

Plain Language Summary

Cold pools are blobs of cold air that can form under thunderstorm clouds due to the evaporation of rain. Because they are denser than the surrounding air, cold pools spread out along the surface. It has long been known that thunderstorm development, while inhibited inside the cold pools, is stimulated near the edges. Here we use idealized numerical simulations of cold pool-producing tropical thunderstorms to study how the cold pools interact to achieve this organization of subsequent clouds. We find that when cold pools collide with one another, they establish a circulation near the surface that lasts for several hours. This circulation transports air from a very large area into a small one, where it is deflected upward and eventually facilitates thunderstorm development. Our results improve our understanding of how cold pools trigger extreme rain events and have implications for how thunderstorms should be depicted in climate models.

1. Introduction

Cold pools (CPs) form when a fraction of convective precipitation reevaporates as it falls to the surface. The latent heat absorbed during the phase change cools the atmosphere below cloud base, creating a body of relatively dense air that sinks to the ground and spreads laterally. CPs can spread over distances of tens to hundreds of km in the course of one day (Zuidema et al., 2017) and can modify the conditions for subsequent convection by creating and transporting anomalies in temperature, moisture, and wind (e.g., Böing et al., 2012; de Szoeke et al., 2017; Droegemeier & Wilhelmson, 1985; Feng et al., 2015; Khairoutdinov & Randall, 2006; Knippertz et al., 2009; Terai & Wood, 2013; Torri & Kuang, 2016; Tompkins, 2001). The edges, where the CPs meet and interact with ambient boundary layer air, are commonly referred to as the *outflow boundaries*.

Deep convective cells have long been known to preferentially form along these outflow boundaries (Droegemeier & Wilhelmson, 1985; Purdom & Marcus, 1981), and two mechanisms explaining this have been proposed. The classic and intuitive view is that forced lifting along the advancing outflow boundaries helps low-level air parcels overcome convective inhibition (CIN) and reach the level of free convection (LFC) (Droegemeier & Wilhelmson, 1985; and more recently, Jeevanjee & Romps, 2015; Torri et al., 2015). This view was challenged by Tompkins (2001). In cloud-resolving model simulations of a tropical ocean environment, he observed that convective triggering occurred long *after* the expansive phase of the CPs, which is when the highest wind speeds at the outflow boundaries occur. The key to triggering new deep convection is therefore attributed to a combination of low CIN and high convective available potential energy (CAPE) at the outflow boundary after the CP cold anomaly was removed by surface fluxes, a mechanism that has found support in later studies (Langhans & Romps, 2015; Torri et al., 2015).

Colliding outflow boundaries create bands of strong updrafts (Böing et al., 2012; Lima & Wilson, 2008; Wilson & Schreiber, 1986), typically explained by either or both of the above mechanisms. Due to low-level convergence, these bands constitute moist patches over which clouds form (Krueger, 1988). Schlemmer and Hohenegger (2014) showed that larger moist patches support the formation of more, as well as larger and deeper clouds. This lends support to the "near-environment hypothesis" postulated by Böing et al. (2012), stating that wider cloud bases over colliding outflow boundaries reduce the entrainment of subsaturated air into growing clouds, thus allowing them to retain their buoyancy and develop into cumulonimbi.

Pursuing these findings, Feng et al. (2015) used high-resolution regional model simulations of warm tropical ocean conditions to examine convective organization by CPs. They reported colliding CPs to trigger substantially more shallow convection than isolated ones, a finding attributed to enhanced updraft velocities. The increased accumulation of shallow convective clouds, in turn, moistened the environment above the boundary layer, reducing dry-air entrainment and eventually allowing for deep convection to develop. This echoes an earlier study by Waite and Khouider (2010), which found the deepening of cumulus clouds in cloud-resolving numerical experiments to depend heavily on the detrainment of moist air into the environment by congesti preceding the formation of deep convection.

Parameterizations of convection in climate models have struggled to capture the diurnal cycle of convection occurring over tropical land (e.g., Betts & Jakob, 2002; Nesbitt & Zipser, 2003). Coupling a convection parameterization scheme with a simple representation of CPs that dynamically allow surface parcels to overcome convective inhibition amended this (Grandpeix & Lafore, 2010; Rio et al., 2009), suggesting that forced lifting by CPs actively organizes convection over land.

Convective conditions over tropical oceans differ from those over land due to the larger heat capacity of the sea surface. The tropical marine atmosphere is therefore subject to near-constant surface heating and is often approximated as residing in a state of radiative-convective equilibrium (RCE) which cannot produce a diurnal cycle of convection. Thus, there is reason to believe that the ways in which CPs organize and trigger convection are also different, as the results of, for example, Tompkins (2001) examplify.

Which mechanisms are behind triggering of deep convection under which conditions is still contested in the literature. In any case, CPs doubtlessly are a key ingredient in the organization of convection and the transition from shallow to deep convection. In this study, we characterize the causality between CPs and subsequent convection under approximate RCE conditions using large-eddy simulations (LES). To do so, we exploit an idealized setup that permits a simple tracking of the convergence zones established by colliding outflow boundaries. Furthermore, we ask what the contribution of surface fluxes is to the moisture convergence.

2. Methodology

2.1. Large-Eddy Simulations

Idealized large-eddy simulations (LES) are run using the University of California, Los Angeles (UCLA) LES code (Stevens et al., 2005). Parameterizations of cloud microphysics and surface energy fluxes (supporting information Text S1, Pincus & Stevens, 2009; Seifert & Beheng, 2006; Smagorinsky, 1963; Stevens, 2010) make the model suitable for studying cold pools (e.g., Haerter et al., 2017; Henneberg et al., 2020; Moseley et al., 2016). The main aim of this study is to better understand the processes leading to deep convective triggering under RCE conditions. To test the robustness of the results, we perform three simulations with a varying surface boundary condition: a control simulation (termed CTR) with a surface at 300 K and 100% relative humidity, compared to a simulation with a 2 K colder surface (termed −2K) and a simulation with a surface evaporation reduced to 70% (termed RH70) (Haerter & Fuglestvedt, 2020). CTR and −2 K correspond to tropical ocean conditions (Bowen ratios of ∼0.1), while the Bowen ratio in RH70 (∼0.25) resembles conditions over tropical rainforests (e.g., Wallace & Hobbs, 2006).

To achieve radiative convective equilibrium (RCE), surface temperature and humidity, as well as insolation are held constant throughout each simulation. We here study the properties within RCE, attained after 300 model hours for CTR and −2K, and 150 model hours for RH70 (Figure S1). These temporal thresholds were chosen as the times when the spatial averages of low-level temperature and humidity were converged to the equilibrium values (Text S1, Haerter & Schlemmer, 2018).

2.2. Idealized Setup

Focusing on diurnal cycle dynamics, Haerter et al. (2019) highlights the complexity of CP interactions within the three-dimensional atmosphere. In that case, several geometrical configurations of CP collisions can occur, and those involving two and three CPs were found to be conceptually different. In order to remove the complexities introduced by the different geometries of collision, and focus entirely on the processes that are active in the lead-up to the formation of new convective events after a collision, we here use an idealized setup: the LES is run at a 200 km × 5 km horizontal domain size and the output averaged over the narrow dimension before analysis. This pseudo-2-D setup hence resembles air embedded in a channel, where spreading CPs are forced to travel along the direction of the channel. This is enforced by the laterally periodic boundary conditions, as a CP's outflow along the narrow dimension will soon collide with the same CP's opposite edge, effectively limiting the direction of motion to be along the long dimension (Text S2).

2.3. Simple Tracking of Outflow Boundaries

An advantage of the idealized setup is that the causality between colliding outflow boundaries, loci of convergence, and subsequent deep convection becomes apparent. In order to study the evolution of the atmosphere at the loci of convergence in the hours leading up to a new convective event, a tracking algorithm is used: our algorithm identifies these loci preceding every deep convective precipitation event.

We identify each deep convective precipitation event as an object extending a maximum of 4 km in each direction and lasting for a maximum of 160 min from the time and position of precipitation onset. These values were chosen as a compromise between the typical extents of precipitation events and the typical spacing between them (Figure S2). Precipitation onset is defined as the time of the first local precipitation intensity maximum in the spatial dimension of each such object that exceeds 1 mm hr^{-1}. The tracking algorithm identifies the loci of convergence backward in time from the precipitation onset of each event. The loci of convergence are defined as the maxima of low-level vertical velocity, searching in the vicinity of the last point on the track. This vicinity is chosen as the area within 1.6 km in each direction from the last point, in effect assuming that the convergence locus is not advected further in a single output time step, corresponding to an advection speed of ∼2.7 m s^{-1} (Figure S2). The search is terminated when the track leads to a preceding deep convective precipitation event. If this condition is not met, the search is terminated when the tracking exceeds 80 ten-minute output time steps, corresponding to 13.3 model hours.

3. Results

3.1. Identifying Precipitation Events and Convergence Loci

To understand the CP dynamics in the present channel domain, it is instructive to focus on a specific vertical model level and consider any output field within the horizontal coordinate as well as time (Figures 1a–1c). CPs travel along the surface and their outflow boundaries are visible as sharp spikes of positive vertical velocity. These spikes correspond to sharp gradients in horizontal velocity, that is, loci of strong horizontal convergence. The convergence patterns are mirrored by the patterns in low-level moisture, with water vapor mixing ratio increasing near the colliding outflow boundaries, or "collision fronts" (Figure 1b). Inspecting this convergence pattern further, it is apparent that the collision fronts are also the locations where new deep convection events occur (Figure 1c). Although outflow boundaries cause large vertical velocities as they collide, inspection shows that new events typically occur at the collision front several hours after the collision occurred. This suggests that the immediate mechanical lifting of boundary layer parcels to the LCL plays little role in the triggering of new events in RCE. Instead, we here argue that the circulation surrounding the collision front continues long after the time when the outflow boundaries initially collide, allowing moist low-level air to be continuously lifted within the convergence zone.

To qualitatively appreciate this, the moisture circulation during two phases of a CP's lifetime is plotted in Figures 1d and 1e. Strong vertical velocities accompany the horizontal velocities at the outflow boundary during the early expansive phase (Figure 1d). Note the two areas of enhanced moisture (highlighted by white arrows in Figure 1d), which are surrounded by a circulation mixing moist surface air back toward the cold pool wake. These moisture anomalies are associated with the vortex rings formed by the expanding density current (Lundgren et al., 1992) and have the effect of moistening the upper boundary layer at heights of 800 to 1,000 m. This moistening effect is also evident from Figure 1e, where the moisture anomaly is located behind, rather than ahead of, the cold pool vortex ring.

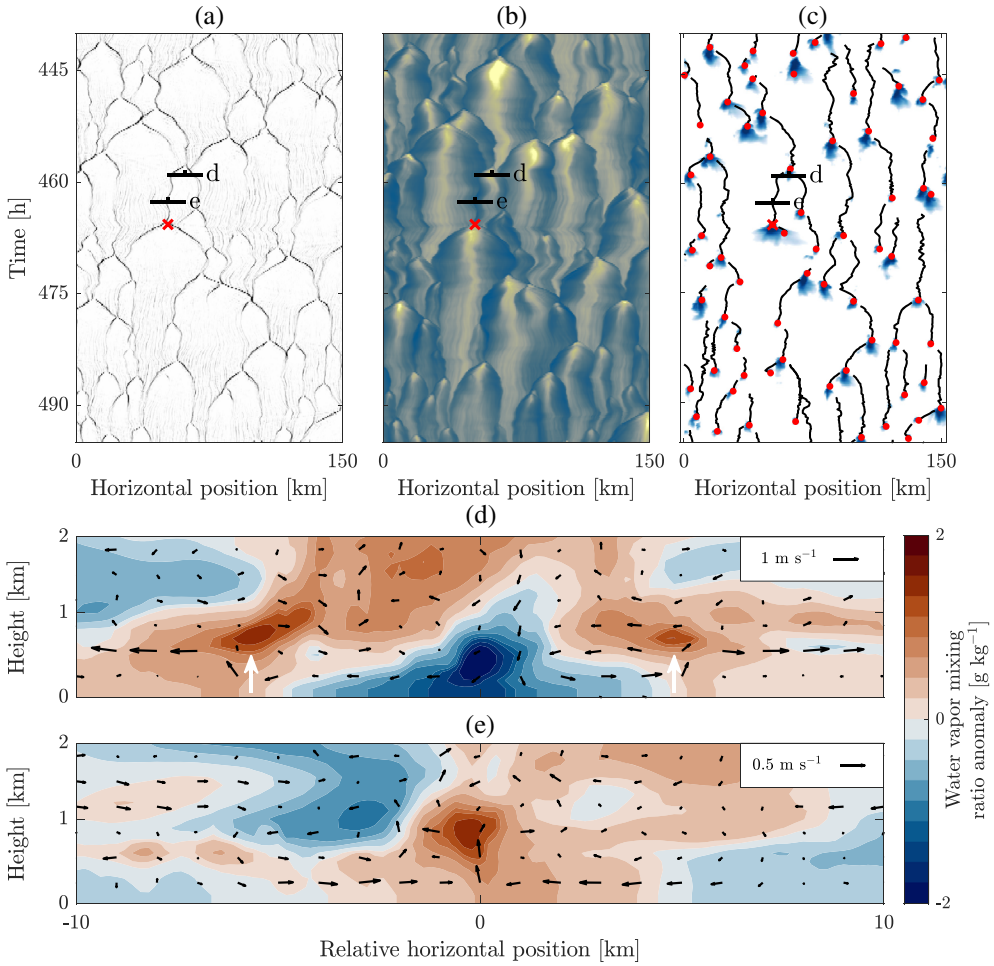

Figure 1. Cold pool dynamics in the LES (CTR experiment). (a) 100 m vertical velocity. Dark shades indicate positive values. (b) 50 m water vapor mixing ratio. CP interiors are dry (yellow), and outflow boundaries moist (blue) (same color axis as in Figure 3a). (c) Simple tracking of precipitation events (red dots) and preceding convergence loci (black lines) plotted over precipitation intensity (blue shading). Red x marks the time and position of the precipitation event analyzed in Figure 3. Black horizontal lines mark times and positions of vertical cross sections plotted in panels (d) and (e). (d, e) Vertical cross sections of water vapor mixing ratio anomaly (contours) relative to the steady state average and wind (vectors), centered on a recently formed cold pool 1 hr after precipitation onset (d) and its left resulting collision front 4 hr 40 min after (e). For clarity, the wind is subtracted by the horizontal mean flow in the plotted subdomain, and velocities are averages of bins of 5 and 3 grid points (corresponding to 100 and 30 m) in the horizontal and vertical dimension, respectively. Positive moisture anomalies associated with the cold pool's outflow boundaries are highlighted by white arrows in (d).

Even more than 4 hr after the outflow boundary has been stalled by that of the neighboring CP, moisture continues to circulate, converging at the collision front, where it is advected to higher levels and constitutes a moisture anomaly (Figure 1e). This convergence continues for several hours at approximately the same position before a new deep convection event occurs.

To show that such sustained CP-induced convergence zones are the most important mechanism behind organizing deep convection in the numerical experiments, we use the tracking algorithm (section 2.3) to aggregate the loci of these convergence zones in the buildup to deep convection events.

3.2. Aggregate Statistics During Event Buildup

In our idealized setup the tracking of convergence loci preceding deep convection permits sampling of the local atmospheric properties. Note that in three-dimensional analogs such tracking would be far more cumbersome (Henneberg et al., 2020): outflow boundaries would be line structures and the cross section upon collision of any two or more outflow boundaries would have far more complex geometries than in the case we study here—introducing additional degrees of freedom into the analysis.

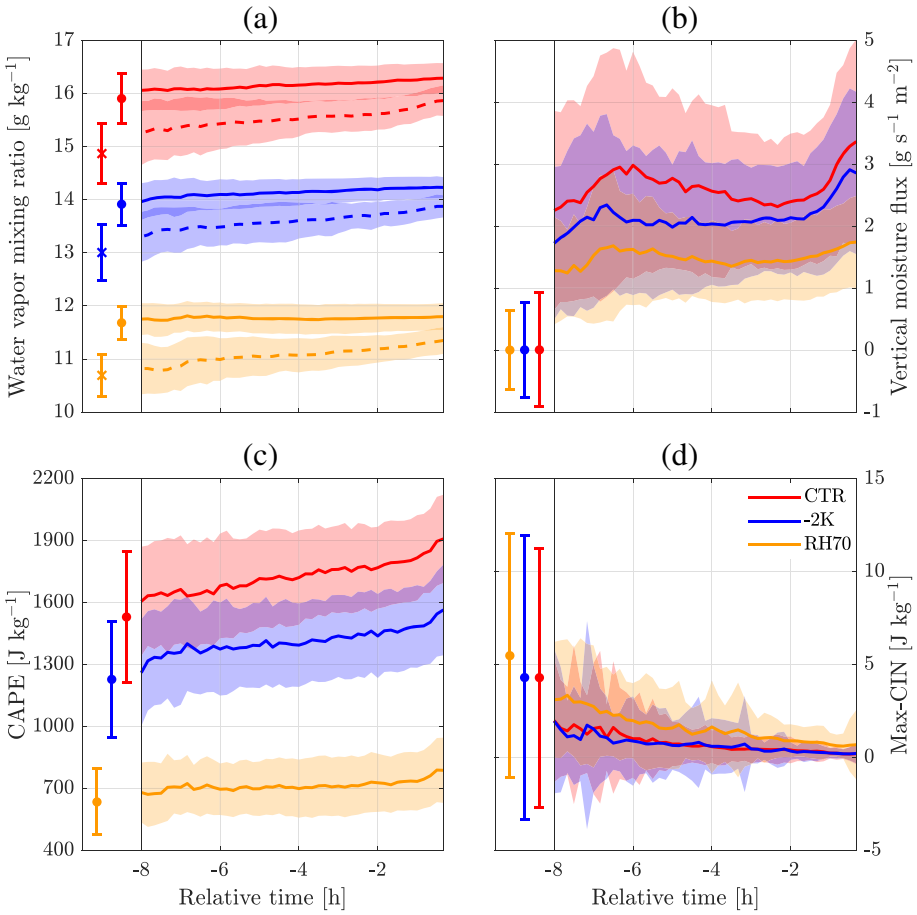

Figure 2. Time evolution of aggregate atmospheric properties at the tracked convergence loci. The time axis is relative to the precipitation onset at 0 hr. (a) Water vapor mixing ratio at 50 m (solid) and at the mean level of free convection ($\overline{\text{LFC}}$) (dashed). (b) 100 m vertical moisture flux ($qw\rho$). (c) Convective available potential energy (CAPE). (d) Convective inhibition (CIN) for the most inhibited boundary layer reference parcel ($z \leq \overline{\text{LFC}}$). Solid/dashed lines are mean values and shading indicates one standard deviation of the aggregate. Left-side markers and errorbars show the system mean values and one standard deviation for the plotted quantities (dot and x correspond to solid and dashed, respectively).

Using the backtracking for all detected deep convective events, we recover the history of instability and moisture during the time leading up to the event (Figure 2). The track duration, that is, the time between precipitation onset and the time when the backtracking is terminated, differs from event to event. For the aggregate buildup a duration starting at −8 hr is chosen, as the frequencies of track durations longer than this drop below 5% for all three numerical experiments (Figure S3). At the other end, the aggregate buildup is truncated at 20 min before precipitation onset. We do this because the increase/decrease of the quantities plotted in Figure 2 see a sudden reversal at this time (Figure S4). We attribute this reversal to the effects of downdrafts forming in the minutes before the identified precipitation onset. This time window of −8 hr to −20 min is used for the results reported in Table 1.

Classical measures of convective instability are CAPE and CIN (*Definition*: Text S3). Indeed, CAPE (Figure 2c) is appreciable and increases systematically before event onset. CIN requires a more careful inspection, as parcels at the lowest model level show very small values of CIN ≈0 throughout the lead-up to the new event. Accompanied by the appreciable CAPE, this lack of inhibition implies deep convection onset according to parcel theory. To evaluate the maximum inhibition in the boundary layer, we define the boundary layer as bounded above by the mean LFC in each experiment ($\overline{\text{LFC}}$) and pick the most stable parcel, for which convective inhibition henceforth is termed *max-CIN*. Max-CIN reveals that a weak inhibition persists in the boundary layer but sees a gradual reduction during the buildup (Figure 2d). The reduction in max-CIN indicates that the higher levels of the boundary layer, where the most inhibited parcels typically reside, are affected by the low-level convergence over the course of hours.

Table 1
Aggregate Statistics During Event Buildup[a]

	CTR	−2 K	RH70	Unit
Δq(50 m)	0.2 ± 0.5	0.3 ± 0.4	0.0 ± 0.4	g kg^{-1}
$\Delta q(\overline{\text{LFC}})$	0.6 ± 0.7	0.6 ± 0.5	0.5 ± 0.5	g kg^{-1}
IVMF(100 m)	74 ± 6	61 ± 5	42 ± 3	kg m^{-2}
IVMF($\overline{\text{LFC}}$)	60 ± 10	49 ± 9	23 ± 5	kg m^{-2}
Model level of $\overline{\text{LFC}}$	600	600	1,102.5	m

[a]Mean ±1 standard deviation.

Figure 2a shows that low-level moisture increases modestly along the collision front until new deep convection sets in, whereas the increase at the $\overline{\text{LFC}}$ is several times larger (Δq, Table 1). As can be seen in Figure 2b, the low-level vertical moisture flux (= $qw\rho$, where q is water vapor mixing ratio, w is vertical velocity, and ρ is the density of air) remains positive for the duration of the buildup, advecting large quantities of water vapor over the 8 hr. Integrating this quantity over the buildup yields the time-integrated vertical moisture flux (IVMF) (Table 1). IVMF($\overline{\text{LFC}}$) is ∼80% of IVMF(100 m) in CTR and −2 K, and ∼55% in RH70, indicating that the majority of the moisture converging at the lowest levels makes it out of the boundary layer.

The results above demonstrate a pattern in the buildup to deep convection that is consistent across the three simulations: A weak inhibition in the boundary layer is gradually removed over the convergence locus, eventually setting off deep convection and releasing the ample CAPE. Concurrently, moisture is being directed up and out of the boundary layer by the low-level convergence. In the following section, we turn to study the source of this moisture, the eventual moistening of the atmosphere, as well as the means of removing max-CIN during the buildup.

3.3. The Origin and Fate of Converging Moisture

It is straightforward to compute the accumulated horizontal moisture convergence, C, at vertical level z between time t_i and t_f, by considering the time-integrated difference

$$C \approx \frac{\rho(z)\delta z(z)\Delta t}{x_r - x_l} \sum_{t=t_i}^{t_f} \left(q(z, x_l, t) v_h(z, x_l, t) - q(z, x_r, t) v_h(z, x_r, t) \right), \quad (1)$$

where Δt is the time increment, $q(z, x, t)$ is the water vapor mixing ratio at horizontal position x and time t, $v_h(z, x, t)$ is the corresponding horizontal velocity, x_l and x_r are the horizontal positions of the left and right boundaries defining the convergence zone, here taken to be 2 km to either side of the convergence locus, $\delta z(z)$ is the vertical grid spacing, and $\rho(z)$ is the air density.

To quantify how much of the moisture increase is due to surface moisture fluxes, we repeat the calculation in Equation 1, but replace $q(x_l, t)$ and $q(x_r, t)$ by $q(x'_l, t'_l)$ and $q(x'_r, t'_r)$, where the transformed values x' result from x by iterative backtracking:

$$x(t - \delta t) \rightarrow x(t) - \delta t \, v_h(x, t) \, , \quad (2)$$

where $\delta t > 0$ is chosen sufficiently small. This backward advection is repeated $n \equiv (t - t')/\delta t$ times, the required number of iterations to reach (x', t'), the location and time of the preceding downdraft on each side of the convergence zone. This procedure essentially replaces the value of q of a parcel at the convergence zone boundary by the value of q at the position where the parcel entered the lowest model level. This would be the value of q if no surface fluxes were present during the parcel's journey toward the convergence zone. We can assume that the parcel is only advected horizontally, as vertical velocities contribute little (∼2%) to the wind speed in the regions that are neither convergence zones nor downdrafts (Figure S5). The difference in moisture convergence between using $q(x, t)$ and $q(x', t')$ approximates the surface flux contribution in the time between formation of CPs and the event they trigger.

Figure 3a shows this analysis conducted on a case in CTR (same as Figures 1d and 1e). The parcels at the boundaries of the convergence zone follow paths originating in the dry centers of the preceding left and right CPs. The low-level circulation set up by the CPs (Figure 3b) transports boundary layer air into the convergence zone, where the convergence deflects it vertically. Note that the horizontal low-level velocities

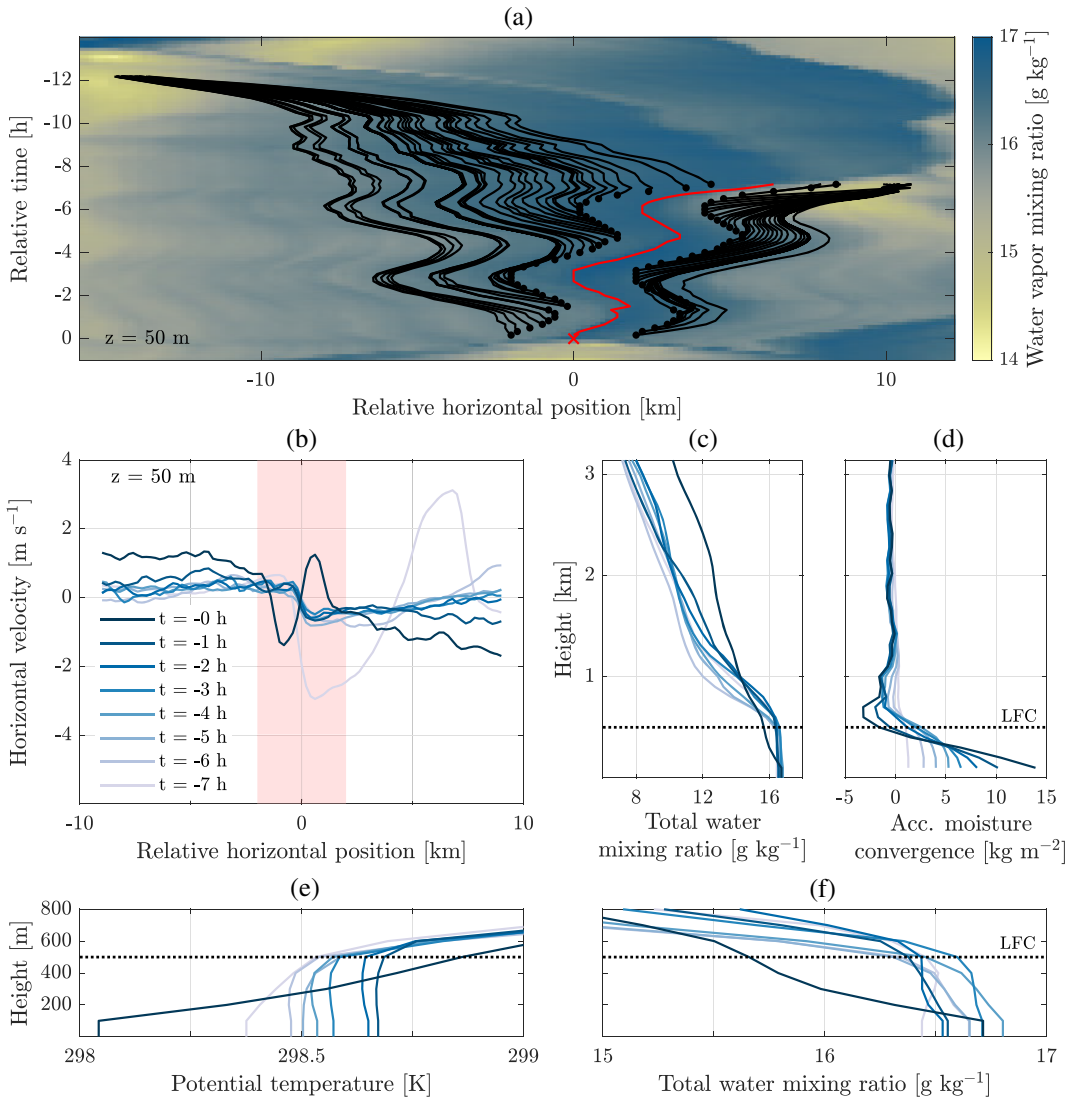

Figure 3. Identifying the contribution from surface moisture fluxes to a deep convection event in CTR. (a) 50 m water vapor mixing ratio. Positions of parcels (black dots) in the vicinity of the convergence locus (red line) preceding a deep convection event (red x) advected backward in time (black lines) to origins in previous downdrafts. Position is relative to the precipitation event. (b) Time evolution of the horizontal profile of 50 m horizontal wind. Position is relative to the convergence locus. Faint red shaded rectangle indicates the area taken as the convergence zone bounded by the black dots in (a). (c) Time evolution of the vertical profile of total water mixing ratio at the convergence locus. (d) Time evolution of the vertical profile of accumulated horizontal moisture convergence, where the convergence is approximated according to Equation 1. (e, f) Analogous to (c) but for potential temperature (e) and total water mixing ratio (f) in the lowest 800 m.

are directed toward the convergence zone for several kilometers to each side, maintaining a large "catchment area" for the convergence zone. This leads to a moistening throughout the atmospheric column over the convergence zone during the buildup to the new deep convective event (Figure 3c). Using Equation 1 to approximate the low-level accumulated horizontal moisture convergence beginning from the earliest time that the convergence locus is identified, shows that the moisture converges below the local LFC at 500 m (Figure 3d). Moisture convergence above this level is negative despite the increase in total water mixing ratio, implying that moisture is vertically advected out of the boundary layer before being detrained into the environment. The total low-level moisture convergence over the duration of the lead-up amounts to 13.9 kg m^{-2}. Using instead the values $q(x', t')$, found by iterative backtracking, in the calculation of low-level moisture convergence, the amount is 13.0 kg m^{-2}. The small difference of 0.9 kg m^{-2} shows that moisture

fluxes contribute little (~6%) to the total moisture entering the convergence zone in the time between CP formation and subsequent event.

The partitioning into advective and moisture source contributions shows that the circulation set up by the colliding outflow boundaries, which persists for hours, acts as "moisture conveyor belts" on either side of the convergence zone. These conveyor belts extend ~10 km to the sides, approximately corresponding to the radii of the associated CPs. Over the duration of the buildup, the velocities increase, especially in the final hours (Figure 3b). This suggests that the circulation initiated by the CPs sustains and amplifies itself through convection over the convergence locus.

Note that the analysis above considers the convergence of moisture during the time between the onset of the new event and the CP formation under the preceding event to the right, illustrated by the red line in Figure 3a. As can be seen, a moist patch is already present at the beginning of this time interval, which can explain the discrepancy between the 13.9 kg m^{-2} that enter the convergence zone through advection and the almost four times higher average low-level vertical moisture flux observed at the aggregate convergence loci (Table 1). The presence of a moist patch highlights how each deep convective event cannot be considered independent from processes that occurred in the more distant past. Rather, moisture is continuously "funneled" into localized patches by the CPs from many previous deep convection events - thus jointly predetermining the locations of subsequent events.

Whereas moisture convergence implies that the upper boundary layer is gradually moistened, moisture alone is not sufficient to explain the removal of max-CIN (Figure 2d). We therefore consider both the temperature and moisture changes occurring in the boundary layer during the event buildup (Figures 3e and 3f). We examine the relative contributions to buoyancy, which are well-approximated by the changes to virtual potential temperature $\theta_v(\theta, q) = \theta(1 + q/\epsilon)(1 + q)^{-1}$ with θ, the potential temperature, and $\epsilon \approx 0.622$, the ratio of the gas constants of air and water vapor. Expanding θ_v to first order in $q' \equiv q_f - q_i$ and $\theta' \equiv \theta_f - \theta_i$ with the subscripts i and f denoting, respectively, the initial and final values of the quantities during event buildup, then

$$\theta_v' \equiv \theta_v(\theta_f, q_f) - \theta_v(\theta_i, q_i) = \frac{\partial \theta_v}{\partial q}|_{\theta_i, q_i} q' + \frac{\partial \theta_v}{\partial \theta}|_{\theta_i, q_i} \theta' + \mathcal{O}(q'^2, \theta'^2, q'\theta') \, . \tag{3}$$

To quantify the contributions from water vapor and temperature changes, that is, the two first terms on the right-hand side of Equation 3, we evaluate the partial derivatives to yield

$$\frac{\partial \theta_v}{\partial q}|_{\theta_i, q_i} = \theta_i \frac{1 - \epsilon}{\epsilon(1 + q_i)^2} \approx 176\text{K}, \tag{4}$$

$$\frac{\partial \theta_v}{\partial \theta}|_{\theta_i, q_i} = \frac{q_i + \epsilon}{\epsilon(1 + q_i)} \approx 1 \, . \tag{5}$$

Using $q' \approx 0.2$ g kg^{-1} and $\theta' \approx 0.2$ K (Figures 3e and 3f) in Equation 3, the contributions from moisture and temperature changes are, respectively, 0.04 and 0.2 K, that is, approximately a factor five difference. Hence, the temperature contribution to buoyancy within the boundary layer dominates the removal of max-CIN before the new event is set off. For the case in Figure 3, max-CIN is found for parcels at $z = 400$ m, and the LFC for these parcels is at $z = 500$ m. Crudely approximating the change in max-CIN, assuming a linear relaxation in θ_v' between these two levels, yields $g\, \delta z\, \theta_v'/\theta_{v,i} \approx 1$ J kg^{-1}, where g is the acceleration due to gravity and $\delta z = 100$ m the layer thickness, commensurate with the removal of max-CIN observed in Figure 2d.

4. Discussion

Our results point to a continuous premoistening of the atmospheric column over convergence zones. These convergence zones are established by colliding CPs that spread away from previous deep convective events. The resultant moisture dynamics, which occurs over several hours, is part of an overturning circulation which intuitively resembles a conveyor belt transporting moisture to the location of the new deep convective event.

Our results resonate in part with mechanisms hypothesized in previous studies. The near-environment hypothesis (Böing et al., 2012; Schlemmer & Hohenegger, 2014) is by Feng et al. (2015) described as a preconditioning acting through an increased number of shallow clouds that shield deepening clouds from the subsaturated environment. They argue that these shallow clouds are a result of the dynamical forcing along collisions fronts, based on the occurrence of higher vertical velocities over colliding outflow boundaries. However, our results draw focus instead to the low-level circulation set up by the CPs. Rather than the preconditioning aloft being controlled by the strength of forced uplift in the expanding phase of the CPs, we find that the slow and consistent moisture convergence near the surface establishes long-lasting convergence zones, constituting moist patches (Schlemmer & Hohenegger, 2014), that in turn moisten the atmosphere above. Thisresonates better with the second idea put forward by Böing et al. (2012), the "time scale hypothesis," which suggests that the role of the subcloud layer is to establish updrafts lasting long enough to permit cloud deepening. As they point out, these loci will be subject to a positive feedback, as once deeper clouds form, they will amplify the convergence beneath them and further improve the conditions for deep convection. Whether this convergence zone is maintained by the original CP circulations or by this positive feedback is up for debate, but we interpret the current results to demonstrate that colliding outflow boundaries are necessary to initialize the circulation.

The type of "pseudo-2-D" geometric setup exploited in the present study helps to clarify the causality between CPs, moisture convergence, and subsequent deep convection, and permits a simple way of tracking it. We suggest that the mechanisms at work in the setup may also apply in the 3-D analog, where the horizontal dimensions would be of equal scale. The basic notion that each deep convection event should on average spawn one new one necessarily holds true in the 3-D case as well. This is an inevitable consequence of considering an RCE state, where the number of simultaneous events is constant. However, there are subtle differences between the 2-D and 3-D cases: as discussed earlier (section 2.2, Text S2) a 3-D domain permits both 2CP and 3CP collisions, whereas in the current setup CPs are confined to move along only one horizontal dimension. All collisions in the channel domain effectively act like 3CP collisions in a 3-D domain, since the air trapped between any two colliding CPs in the channel is forced to escape vertically. Thus, the dynamical effect of CP collisions could be overestimated (Figure S6). Even then, our findings suggest that the immediate forced lifting in the moment when CPs collide is incapable of triggering deep convection and that the slower process of funneling moisture into convergence zones dominates in RCE.

As a final remark, it is important to emphasize that the surface fluxes in the LES are parameterized using Monin-Obukhov similarity theory (section 2.1), which assumes a constant-flux-layer between the surface and the lowest model level. With the resolution and staggered grid used in the current study, this level is located at 50 m. The reader should note that our results rest on the ability of the LES to parameterize the surface fluxes, an aspect that could be investigated systematically in further studies.

5. Summary and Conclusions

This study aimed to clarify the mechanisms with which CPs organize and initiate new deep convection events in RCE. Large-eddy simulations run in an idealized 2-D-like setup elucidate the causal relationships between CPs, moisture convergence, and deep convection triggering: where outflow boundaries collide, the interaction of the circulation within each CP establishes narrow convergence zones in the boundary layer that persist for hours, sustained by "conveyor belts" of moisture on either side.

As moisture from a several kilometers wide "catchment area" is advected into the convergence zone and deflected vertically, the atmosphere above gradually moistens. Tracking the loci of convergence shows that the aggregate convergence locus experiences weak CIN and large CAPE already several hours before deep convection occurs. The inhibition is present in the upper levels of the boundary layer and is gradually removed over the duration of the buildup, eventually permitting deep convection. The low-level vertical moisture flux remains positive, ~1–3 g s^{-1} m^{-2} depending on the surface boundary condition, over the whole duration, steadily increasing the water vapor mixing ratio above the boundary layer.

The mechanism described above is illustrated by a closer analysis of a single deep convection event and its buildup in the large eddy simulation. We find that the CPs on either side preceding the event establish a circulation where air in the lowest levels is funneled into a narrow convergence zone from an area ~10 km to either side. The convergence removes inhibition by warming all levels of the boundary layer within the

convergence zone. During the time between the formation of the preceding CPs and the event, the contribution of surface moisture fluxes to the total moisture that enters the convergence zone is relatively small (6%). In the convergence zone, the converging moisture inevitably ascends and leads to a moistening of the atmospheric column despite horizontal moisture divergence above the boundary layer. Together, our results support the notion of gradual preconditioning of the atmosphere above convergence zones established by colliding outflow boundaries.

Data Availability Statement

LES data used in this paper are archived and available on the NIRD Research Data Archive (https://doi.org/10.11582/2020.00008).

Acknowledgments
H. F. F. and J. O. H. gratefully acknowledge funding by a grant from the VILLUM Foundation (Grant 13168) and the European Research Council (ERC) under the European Union's Horizon 2020 research and innovation program (Grant 771859). We acknowledge the Danish Climate Computing Center (DC3).

References

Betts, A. K., & Jakob, C. (2002). Evaluation of the diurnal cycle of precipitation, surface thermodynamics, and surface fluxes in the ecmwf model using lba data. *Journal of Geophysical Research*, *107*(D20), 8045. https://doi.org/10.1029/2001JD000427

Böing, S. J., Jonker, H. J., Siebesma, A. P., & Grabowski, W. W. (2012). Influence of the subcloud layer on the development of a deep convective ensemble. *Journal of the Atmospheric Sciences*, *69*(9), 2682–2698.

de Szoeke, S. P., Skyllingstad, E. D., Zuidema, P., & Chandra, A. S. (2017). Cold pools and their influence on the tropical marine boundary layer. *Journal of the Atmospheric Sciences*, *74*(4), 1149–1168.

Droegemeier, K. K., & Wilhelmson, R. B. (1985). Three-dimensional numerical modeling of convection produced by interacting thunderstorm outflows. part I: Control simulation and low-level moisture variations. *Journal of the Atmospheric Sciences*, *42*(22), 2381–2403.

Feng, Z., Hagos, S., Rowe, A. K., Burleyson, C. D., Martini, M. N., & de Szoeke, S. P. (2015). Mechanisms of convective cloud organization by cold pools over tropical warm ocean during the amie/dynamo field campaign. *Journal of Advances in Modeling Earth Systems*, *7*, 357–381. https://doi.org/10.1002/2014MS000384

Grandpeix, J.-Y., & Lafore, J.-P. (2010). A density current parameterization coupled with Emanuel's convection scheme. Part I: The models. *Journal of the Atmospheric Sciences*, *67*(4), 881–897.

Haerter, J. O., Berg, P., & Moseley, C. (2017). Precipitation onset as the temporal reference in convective self-organization. *Geophysical Research Letters*, *44*, 6450–6459. https://doi.org/10.1002/2017GL073342

Haerter, J. O., Böing, S. J., Henneberg, O., & Nissen, S. B. (2019). Circling in on convective organization. *Geophysical Research Letters*, *46*, 7024–7034. https://doi.org/10.1029/2019GL082092

Haerter, J., & Fuglestvedt, H. (2020). Large-eddy simulations of radiative-convective equilibrium. Archive2014. Retrieved from https://doi.org/10.11582/2020.00008

Haerter, J. O., & Schlemmer, L. (2018). Intensified cold pool dynamics under stronger surface heating. *Geophysical Research Letters*, *45*, 6299–6310. https://doi.org/10.1029/2017GL076874

Henneberg, O., Meyer, B., & Haerter, J. O. (2020). Particle-based tracking of cold pool gust fronts. *Journal of Advances in Modeling Earth Systems*, *12*, e2019MS001910. https://doi.org/10.1029/2019MS001910

Jeevanjee, N., & Romps, D. M. (2015). Effective buoyancy, inertial pressure, and the mechanical generation of boundary layer mass flux by cold pools. *Journal of the Atmospheric Sciences*, *72*(8), 3199–3213.

Khairoutdinov, M., & Randall, D. (2006). High-resolution simulation of shallow-to-deep convection transition over land. *Journal of the Atmospheric Sciences*, *63*(12), 3421–3436.

Knippertz, P., Trentmann, J., & Seifert, A. (2009). High-resolution simulations of convective cold pools over the northwestern sahara. *Journal of Geophysical Research*, *114*, D08110. https://doi.org/10.1029/2008JD011271

Krueger, S. K. (1988). Numerical simulation of tropical cumulus clouds and their interaction with the subcloud layer. *Journal of the Atmospheric Sciences*, *45*(16), 2221–2250.

Langhans, W., & Romps, D. M. (2015). The origin of water vapor rings in tropical oceanic cold pools. *Geophysical Research Letters*, *42*, 7825–7834. https://doi.org/10.1002/2015GL065623

Lima, M. A., & Wilson, J. W. (2008). Convective storm initiation in a moist tropical environment. *Monthly Weather Review*, *136*(6), 1847–1864.

Lundgren, T., Yao, J., & Mansour, N. (1992). Microburst modelling and scaling. *Journal of Fluid Mechanics*, *239*, 461–488.

Moseley, C., Hohenegger, C., Berg, P., & Haerter, J. O. (2016). Intensification of convective extremes driven by cloud–cloud interaction. *Nature Geoscience*, *9*(10), 748.

Nesbitt, S. W., & Zipser, E. J. (2003). The diurnal cycle of rainfall and convective intensity according to three years of trmm measurements. *Journal of Climate*, *16*(10), 1456–1475.

Pincus, R., & Stevens, B. (2009). Monte carlo spectral integration: A consistent approximation for radiative transfer in large eddy simulations. *Journal of Advances in Modeling Earth Systems*, *1*, 1. https://doi.org/10.3894/JAMES.2009.1.1

Purdom, J., & Marcus, K. (1981). Thunderstorm trigger mechanisms over the southeast united-states. *Bulletin of the american meteorological society* (Vol.62, pp. 1423–1423). Boston, MA: American Meteorological Society.

Rio, C., Hourdin, F., Grandpeix, J.-Y., & Lafore, J.-P. (2009). Shifting the diurnal cycle of parameterized deep convection over land. *Geophysical Research Letters*, *36*, L07809. https://doi.org/10.1029/2008GL036779

Schlemmer, L., & Hohenegger, C. (2014). The formation of wider and deeper clouds as a result of cold-pool dynamics. *Journal of the Atmospheric Sciences*, *71*(8), 2842–2858.

Seifert, A., & Beheng, K. (2006). A two-moment cloud microphysics parameterization for mixed-phase clouds. part 1: Model description. *Meteorology and Atmospheric Physics*, *92*(1-2), 45–66.

Smagorinsky, J. (1963). General circulation experiments with the primitive equations: I. the basic experiment. *Monthly weather review*, *91*(3), 99–164.

Stevens, B. (2010). Introduction to UCLA-LES. https://www.mpimet.mpg.de/fileadmin/atmosphaere/herz/lesdoc.pdf. (Online; accessed 13-May-2020).

Stevens, B., Moeng, C.-H., Ackerman, A. S., Bretherton, C. S., Chlond, A., de Roode, S., et al. (2005). Evaluation of large-eddy simulations via observations of nocturnal marine stratocumulus. *Monthly Weather Review*, *133*(6), 1443–1462.

Terai, C., & Wood, R. (2013). Aircraft observations of cold pools under marine stratocumulus. *Atmospheric Chemistry and Physics*, *13*(19), 9899–9914.

Tompkins, A. M. (2001). Organization of tropical convection in low vertical wind shears: The role of cold pools. *Journal of the Atmospheric Sciences*, *58*(13), 1650–1672.

Torri, G., & Kuang, Z. (2016). Rain evaporation and moist patches in tropical boundary layers. *Geophysical Research Letters*, *43*, 9895–9902. https://doi.org/10.1002/2016GL070893

Torri, G., Kuang, Z., & Tian, Y. (2015). Mechanisms for convection triggering by cold pools. *Geophysical Research Letters*, *42*, 1943–1950. https://doi.org/10.1002/2015GL063227

Waite, M. L., & Khouider, B. (2010). The deepening of tropical convection by congestus preconditioning. *Journal of the Atmospheric Sciences*, *67*(8), 2601–2615.

Wallace, J. M., & Hobbs, P. V. (2006). *Atmospheric science: An introductory survey*. In (Vol. 92, Chap. 9.2). Burlington, MA: Elsevier.

Wilson, J. W., & Schreiber, W. E. (1986). Initiation of convective storms at radar-observed boundary-layer convergence lines. *Monthly Weather Review*, *114*(12), 2516–2536.

Zuidema, P., Torri, G., Muller, C., & Chandra, A. (2017). A survey of precipitation-induced atmospheric cold pools over oceans and their interactions with the larger-scale environment. *Surveys in Geophysics*, *38*(6), 1283–1305.